

Microstructure, mechanical and wear resistance properties of low-pressure cold-sprayed Al-7 Mg/Al₂O₃ and Al-10 Mg/Al₂O₃ composite coatings

Akisin, C. J., Venturi, F., Bai, M., Bennett, C. J. & Hussain, T.

Published PDF deposited in Coventry University's Repository

Original citation:

Akisin, CJ, Venturi, F, Bai, M, Bennett, CJ & Hussain, T 2021, 'Microstructure, mechanical and wear resistance properties of low-pressure cold-sprayed Al-7 Mg/Al₂O₃ and Al-10 Mg/Al₂O₃ composite coatings', Emergent Materials, vol. (In-press), pp. (In-press).

<https://dx.doi.org/10.1007/s42247-021-00293-4>

DOI 10.1007/s42247-021-00293-4

ISSN 2522-5731

ESSN 2522-574X

Publisher: Springer

Open Access This article is licensed under a Creative Commons Attribution 4.0 International License, which permits use, sharing, adaptation, distribution and reproduction in any medium or format, as long as you give appropriate credit to the original author(s) and the source, provide a link to the Creative Commons licence, and indicate if changes were made. The images or other third party material in this article are included in the article's Creative Commons licence, unless indicated otherwise in a credit line to the material. If material is not included in the article's Creative Commons licence and your intended use is not permitted by statutory regulation or exceeds the permitted use, you will need to obtain permission directly from the copyright holder. To view a copy of this licence, visit <http://creativecommons.org/licenses/by/4.0/>.



Microstructure, mechanical and wear resistance properties of low-pressure cold-sprayed Al-7 Mg/Al₂O₃ and Al-10 Mg/Al₂O₃ composite coatings

C. J. Akisin¹ · F. Venturi¹ · M. Bai² · C. J. Bennett¹ · T. Hussain¹

Received: 3 May 2021 / Accepted: 21 August 2021
© The Author(s) 2021

Abstract

Aluminium alloy-based metal matrix composites have successfully provided effective wear resistance and repair solutions in the automotive and aerospace sectors; however, the design and manufacture of these alloys are still under development. In this study, the microstructure, mechanical properties and wear resistance of low-pressure cold-sprayed Al-7 Mg/Al₂O₃ and Al-10 Mg/Al₂O₃ composite coatings were investigated. The specific wear rates of the coatings were measured when testing them against alumina (Al₂O₃) counterbody, and the results showed that the cold-sprayed Al-10 Mg/Al₂O₃ composite coating showed less wear due to its superior hardness, lower porosity and shorter mean free path compared to the Al-7 Mg/Al₂O₃ composite coating. The microstructural analysis of the worn surfaces of the composite coatings revealed abrasive wear as the primary wear mechanism, and more damages were observed on Al-7 Mg/Al₂O₃ composite coatings. Most notably, Al₂O₃ particles were pulled out from the coating and were entrapped between the Al₂O₃ counterbody and the coating contact surfaces, resulting in a three-body abrasion mode.

Keywords Cold spray · Composite coatings · Wear · Aluminium magnesium alloys · MMC

1 Introduction

As a result of the current rapid technology innovation and economic development, there has been an increase in the demand for lightweight Al alloys with superior mechanical properties in critical industrial sectors such as aerospace and automotive. The fabrication of protective metal matrix composite (MMC) coatings on Al alloys is an effective way to produce high-performance materials as required in these sectors. MMC coatings combine the properties of a ductile metallic matrix and the high strength of a reinforcement phase for a specific performance [1]. Commonly used reinforcement particles in MMC coatings include ceramic particles (Al₂O₃, SiC, B₄C, TiB₂) [2], carbon fibre, synthetic diamond particles [3], carbon nanotubes and graphene [4]. The size, weight fraction and distribution of the reinforcement

particles and the interfacial bonding between the matrix and reinforcement predominately determine the properties of MMC coatings [5]. For example, a higher weight fraction of reinforcement particles and a shorter mean free path between these particles improve the load sharing capacity, hardness and resistance to wear [6].

Various MMC coatings and processing methods have been developed to optimise their microstructure and properties. After half a century of development, a subclass of MMCs, aluminium matrix composite (AMC) coatings, has been widely used in the transport industries due to their lightweight, high strength and good wear resistance [5, 7]. For example, AMCs have been applied on Al 6xxx series used in aircraft floor panels to improve its surface corrosion and wear resistance properties and repair worn-out aerospace gearboxes [8]. Moreover, AMC coatings have recently received increasing attention due to their large potential applications in repair, especially for aircraft and marine components [5]. The various processing techniques that have been used to manufacture AMC coatings include solid-state processing (e.g. powder metallurgy), liquid-state processing (e.g. melt filtration), deposition processing (e.g. plasma spray) and additive manufacturing (e.g. cold spray)

✉ C. J. Akisin
akisinclutus52@gmail.com

¹ University of Nottingham, Nottingham NG7 2RD, UK

² Institute for Future Transport & Cities, Coventry University, Coventry CV1 5FB, UK



[5]. Among these processes, the liquid-state and powder metallurgy techniques have been widely used in industry. Most of these techniques, however, are accompanied by undesirable interfacial reactions, poor interface bonding, high porosity and non-uniform distribution of the reinforcement particles. As a result, the intended superior mechanical properties of AMC coatings are compromised. Therefore, solid-state deposition of AMCs at a temperature below their melting point is needed to retain their desirable properties.

Cold spraying (CS), also known as cold gas dynamic spraying, is one of the additive manufacturing processes for fabricating wear-resistant AMC coatings. CS is a kinetic spray method where metallic feedstock powder particles (typically, 1–50 μm) are deposited in their solid state. Differently from plasma spray and laser powder bed fusion, a coating in CS is formed by the extensive plastic deformation of the metallic powder particles upon impact on the substrate surface, with the temperature of the feedstock well below their melting point [9]. Undesirable interfacial reactions between powder particles and between ductile matrix and the reinforcement, such as oxidation and deleterious high-temperature effects typical of liquid-state processes and thermal spray, are avoided or minimised in CS [10, 11]. The impact velocity of the particles and the properties of the coatings mainly depend on the gas pressure of the cold spray system. Based on the operating pressure, CS has been categorised as either high-pressure or low-pressure cold spray [12].

The low-pressure cold spray (LPSC) technique is a cost-effective method for the fabrication of AMC coatings. In LPSC, compressed air under pressure, not exceeding 1 MPa, is used. At this low pressure, the critical velocity, the threshold velocity of cold-sprayed ductile materials to adhere to the substrate, may not always be reached [12]. However, the shot-peening effect of the impacting reinforcement particles produces compressive stresses on the ductile metallic particles and the previously deposited layer [13]. These compressive stresses increase the denseness of the coating and thus lower the impact velocity needed for deposition of AMCs [14]. Also, the impact of the hard phase reinforcement particles causes the activation of the substrate surface and previously deposited layer by increasing the surface roughness, by creating impressions and craters and disrupting native oxide layers on the substrate surface, promoting the adhesion of incoming particles [13].

The superior properties of cold-sprayed AMC coatings have been attributed to the reinforcement particles content, an increase in weight fraction of the reinforcement particles increases the hardness and wear resistance of the coatings [15]. An optimum reinforcement weight fraction in the feedstock is limited to the range of 20–40% [13]. A larger amount of the reinforcement particles above this trend tends to be detrimental to the coating. Besides, the AMC

composition also contributes to the hardness and wear resistance of the composite coatings [7]. The excellent mechanical and wear resistance properties of various cold-sprayed Al alloys with various types of reinforcement (e.g., Al_2O_3 , B_4C , TiB_2 , SiC) prompted an investigation on the wear resistance performance of Al-Mg alloy composite coatings using the LPSC process.

Al-Mg alloy has drawn much interest recently due to its enhanced mechanical properties, thermal stability and light-weight [16], but Mg is prone to oxidation with conventional additive manufacturing techniques [17], highlighting the need for solid-state manufacturing. Lee et al. [18] reported that an increase in Mg wt% in Al-Mg alloy increases the strength of the alloy. Hassan et al. [19] also reported that an increase in Mg content in Al-Cu-Mg alloy reinforced with SiC ceramic particles increases the hardness and wear resistance of the AMCs.

Cold spraying of AMC coatings have been the subject of previous studies, especially with using the high-pressure cold spray system [7]; however, there is limited research available on low-pressure cold spraying of Al-Mg alloy composite coatings. Therefore, the aim of this study was to develop Al-Mg alloys (Al-7Mg and Al-10Mg) coatings reinforced with alumina particles using a low-pressure cold spray system. The effect of the inclusion of alumina in the feedstock, as well as the effect of the Mg content in the alloy on the mechanical and wear resistance properties, was investigated.

2 Experimental methods

2.1 Materials

The powder feedstocks used for this study were Al-7Mg and Al-10Mg (KITECH[®], South Korea) alloys, and commercially pure (99%) $\alpha\text{-Al}_2\text{O}_3$ (Dycomet, UK) having a particle size of $\text{Dv}10 = 22 \mu\text{m}$ and $\text{Dv}90 = 45 \mu\text{m}$. Each of the alloys was mixed with 40 wt% of the alumina powder using a Turbula[®] mixer operating at a constant speed for 10 min. The size distribution of the Al-Mg alloys powder was measured by laser diffractometry using a Coulter particle size analyser (Beckman Coulter Inc., USA.) equipped with a 750-nm laser. An optical microscope (Nikon Eclipse, Japan) was used to capture the images of the feedstock powders' microstructure.

2.2 Cold spraying

A portable low-pressure Dymet 423 cold spray system (Dycomet, Russia) was used to deposit the Al-7Mg/40 wt% Al_2O_3 and Al-10Mg/40 wt% Al_2O_3 powder blends. The powder blends are labelled as Al-7Mg/ Al_2O_3 and Al-10Mg/

Al_2O_3 , respectively, and their respective coatings labelled as AMC7 and AMC10. To optimise the spray parameters, composite coatings with 20 wt% and 40 wt% of alumina were sprayed on Al 6061 substrates with various parameters: gas pressure was tested at 0.5 and 0.6 MPa and gas preheating temperature at 300 °C, 400 °C and 500 °C, while other parameters were kept constant. The coating deposition efficiency is reflected by the coating thickness, and it was concluded that the coating thickness increased significantly at 40 wt% of alumina, and 0.6 MPa and 500 °C of the gas pressure and temperature, respectively. Thus, these optimised parameters were selected to develop thick coatings. So, with alumina, 40 wt% yielded a good deposition efficiency, 20 wt% yielded a very low deposition efficiency and 0 wt% of Al_2O_3 resulted to no deposition. Higher than 40 wt% of Al_2O_3 can result to lower deposition efficiency which has been reported in [13]. Compressed air was used. The stand-off distance was 5 mm, the transverse speed 60 mm/s and a step size of 2.5 mm for 10 passes in total. The composite powder was fed at 13 g/min. A ceramic nozzle (throat diameter 2.55 mm, exit diameter 4.8 mm, length 138 mm) was used to prevent abrasion from the hard phase Al_2O_3 reinforcement particles.

The coatings were deposited onto 60×25×3 mm Al-6061 T6 substrates (0.99 % Mg, 0.66 % Si, 0.16 % Cr, 0.31 % Cu, 0.08% Mn, 0.25 % Fe, 0.01 % Zn and Al to balance, all in wt%). Before spraying, the substrates were ground using P240 SiC grit paper to promote adhesion of the coating. Each substrate was mounted on a programmable x-y table that allowed a controllable scan pattern and velocity.

2.3 Material characterisation

The coatings were cross sectioned, cold mounted in EpoFin® epoxy resin, ground with P240, P400, P800 and P1200 SiC grit papers and then polished to 1 µm using diamond polish. Final polishing was done with colloidal silica suspension (0.06 µm). Keller's etchant (190 ml H_2O , 5 ml HNO_3 , 3 ml HCl , 2 ml HF) was used to etch the cross sections of the polished samples for 6 s.

The feedstock powder surface morphology and the microstructure of the coating cross sections were captured using an XL30 scanning electron microscope (SEM) (FEI, The Netherlands) operating at 15 kV, both in secondary electron (SE) and back scattered electron (BSE) modes. The elemental composition of the alloy powders was obtained by energy dispersive x-rays spectroscopy (EDX) with the SEM. ImageJ image analysis software (NIH, USA), was used to quantify the porosity, thickness, mean free path and alumina content in the coatings using the greyscale thresholding technique. Five SEM SE images of area 1000 × 1000 µm² were used for measuring the thickness of the coatings, while five lower magnification BSE SEM images of area 300 × 300

µm² were used for measuring the porosity, the volume fraction of alumina retained in the coatings and the mean free path of the coatings. The volume fraction of the alumina in the coating was converted to wt% by using Eq. 1, where V and ρ are the vol% and density of the phase, respectively [15].

$$\text{Wt \% alumina} = \frac{(V_{\text{alumina}} \rho_{\text{alumina}})}{(V_{\text{alumina}} \rho_{\text{alumina}}) + (V_{\text{Al-Mg}} \rho_{\text{Al-Mg}})} \quad (1)$$

The density of Al-Mg and Al_2O_3 in this study are taken as 2.7 and 4.0 g/cm³, respectively [15]. The mean free path was evaluated using Eq. 2 [20]:

$$L = \frac{(1 - V_f)}{N_L} \quad (2)$$

where L is the mean free path, V_f is the vol% of the reinforcing particles and N_L is the number of reinforcing particles intercepts per unit length of the test. The value of N_L was evaluated by drawing random straight lines on the image and the number of times that the line intersected an Al_2O_3 particle was recorded. This was recorded a total of 50 times in the five BSE SE images.

X-ray diffraction (XRD) analysis was used to study the phase composition and crystal structure of the alloy powders and composite coatings. XRD analyses of the powders and coatings were conducted on a D8 Advance Da Vinci x-ray diffractometer (Bruker, Germany), with a wavelength of 0.15406 nm (Cu- K_α), in Bragg Brentano θ -2 θ geometry, from 20° to 100° 2 θ , 0.02° step and 0.1 s dwell time. The crystallite size and the lattice parameters of the Al-Mg matrix was analysed using Rietveld refinement (Topas, Bruker, Germany).

2.4 Mechanical properties

The hardness of the alloy powders and matrix in the composite coatings was measured by nanohardness on polished cross sections using a NanoTest P3 nano-indenter (Micro Materials Ltd., UK). A Berkovich indenter was used for the test, with a 20-mN peak load, 3-s dwell time and 4 mN/s loading/unloading rate. This indentation load was chosen after careful selection of the indent size—the distance between the neighbouring indents, as well as the distance between indentation spot and the alumina or Al-Mg matrices, was chosen to be at least twice the lateral size of the indent in order to avoid neighbouring effects when indenting the matrices in the AMC coatings. Ten indentations were performed to obtain an average with standard error.

Vickers microhardness measurements were performed on the Al-6061 T6 substrate and the cross sections of the composite coatings using a Wilson VH3100 microhardness tester

(Buehler, USA). Ten indentations with 10-s dwell time were performed on the cross section of the coatings with a load of 3 N. The microhardness indentation, 3 N (equivalent to about 300 gf) provides indents of a size that is large enough to provide an ensemble value from the alumina particles and Al-Mg alloy matrix, but not too large to incur in boundaries effect from the coating thickness. The final value is presented as an average with standard error.

2.5 Dry sliding wear test

A ball-on-flat rotary tribometer rig (Ducom Europe, The Netherlands) was used to perform dry sliding wear tests on the cold-sprayed composite coatings. The coatings' top surface was ground with P240, P400, P800 and P1200 SiC grit papers, then polished to 1 μm using diamond polish. An alumina ball of 6-mm diameter (Dejay Ltd., UK), with surface roughness $R_a=0.038\text{ }\mu\text{m}$ and Rockwell hardness value of 81, was used as a counterbody. For all wear tests, a load of 10 N, a track diameter of 12 mm and a sliding speed of 0.05 m/s were selected, yielding a total distance of 420 m. Two repeat tests were performed on each sample and the friction coefficient and wear rate data were averaged. The cross-sectional area of the wear track was measured with a Talysurf (Taylor Hobson, France) contact profilometer by averaging eight readings. The wear track depth profile area measured for each test was multiplied by the track diameter to give the wear volume loss. To evaluate the specific wear rate (SWR) of the composite coatings, Eq. 3 was used [21], where V is the wear volume loss in mm^3 , F is the applied load in N and D is the sliding distance in m.

$$\text{SWR} = \frac{V}{FD} \quad (3)$$

The worn surfaces of the coatings and ball were characterised with SEM in the SE and BSE modes. The alumina counterbody wear rate was calculated by assuming the removal of a spherical cap whose radius was measured by OM, according to the method in [22].

3 Results

3.1 Powder and coating characterisation

3.1.1 Powder characterisation

Fig. 1a and c show the SE SEM images of the surface morphology of Al-7 Mg and Al-10 Mg feedstock alloys. The images show a mixture of spherical and irregular shapes in the powders. Also, some satellite particles are present. This event of particle satelliting, which results from interactions of larger particles with smaller particles, is associated

with in-flight contact of molten particle droplets of different sizes under the gas-atomisation production process during the powder production [23]. The particle size distribution of the Al-Mg alloys is displayed in Fig. 1b and d, with $Dv_{10}=9.0\text{ }\mu\text{m}$, $Dv_{50}=18.2\text{ }\mu\text{m}$ and $Dv_{90}=29.9\text{ }\mu\text{m}$ for Al-7 Mg powder, and $Dv_{10}=5.8\text{ }\mu\text{m}$, $Dv_{50}=24.0\text{ }\mu\text{m}$ and $Dv_{90}=48.5\text{ }\mu\text{m}$ for Al-10 Mg, respectively.

To reveal the powder microstructure, cross sections of powder particles were analysed with BSE SEM (Fig. 2a, b) and optical microscopy (Fig. 2c, d). BSE SEM images show a homogeneous contrast indicating good elemental dispersion, with limited porosity and signs of dendritic structure. The dendritic structure is clearly seen in the optical microscope images for both powders. After mixing the Al-Mg feedstock powders with Al_2O_3 reinforcing particles, the composite feedstock material was examined with BSE SEM, as shown in Fig. 3. Here, the Al_2O_3 particles show an angular morphology, and the alloy particles were not damaged by the hard phase Al_2O_3 particles from the powder blending process.

Measurements from the EDX point scan of the Al-Mg feedstock powders' cross sections are shown in Table 1, with 91.2 wt% and 87.8 wt% of Al, and a decrease in the wt% of Mg as expected found in Al-7 Mg and Al-10 Mg, respectively. There are also traces of Mn and a small amount of O in both alloys.

3.1.2 Coating characterisation

Fig. 4 shows the BSE images of cross sections of AMC7 (Al-7 Mg + Al_2O_3) and AMC10 (Al-10 Mg + Al_2O_3) coatings. A dense microstructure with minimal porosity is seen in both coatings with no discontinuity at the coating-substrate interface, suggesting good bonding to the substrate. The measured thicknesses of AMC7 and AMC10 coatings are $(430 \pm 6)\text{ }\mu\text{m}$ and $(650 \pm 8)\text{ }\mu\text{m}$, respectively.

The calculated Al_2O_3 concentration retained in the coatings is $(21.2 \pm 0.4)\text{ wt\%}$ in AMC7 and $(20.8 \pm 0.6)\text{ wt\%}$ in AMC10 coatings. These values are approximately half the weight fraction of Al_2O_3 in the powder blends prior to spraying, which was 40 wt%. However, the difference in the weight fraction of Al_2O_3 retained in the two composite coatings appears negligible. In addition, there is a significant decrease in the measured porosity from $(1.2 \pm 0.1)\%$ in the AMC7 to $(0.4 \pm 0.1)\%$ in the AMC10 coatings.

The SE images of etched cross sections of the composite coatings are shown in Fig. 5. The plastically deformed particles of Al-Mg alloys and the boundaries between Al-Mg alloys and Al_2O_3 particles can be attributed to the severe plastic deformation of the ductile matrix due to the compaction and shot-peening effect of the alumina particles. The images also reveal that the Al_2O_3 particles retained their angular morphology and are surrounded and trapped by the plastically deformed Al-Mg alloy particles. Some of the Al_2O_3 particles were fractured upon deposition, as their

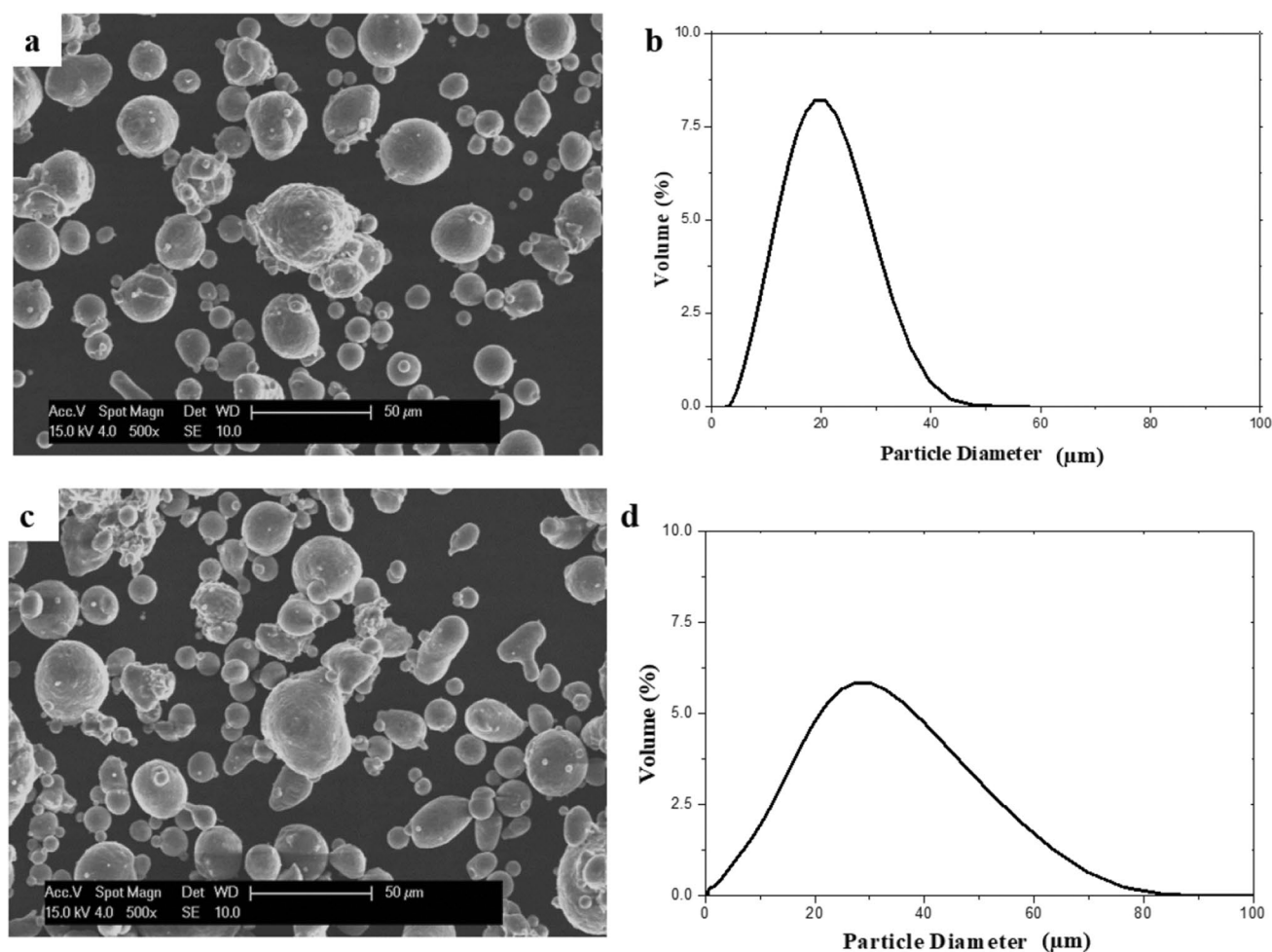


Fig. 1 SE SEM micrographs of the powders' surface morphology **a** Al-7 Mg and **c** Al-10 Mg, and their particle size distribution **b** and **d**, respectively. Some powders are spherical (smaller particles) and

others irregular (larger particles), and some satellites particles are attached to the surface of the larger particles. The mean particle size is 18 μm (**c**) and 24 μm (**d**) with single-peak distribution

size is smaller than the initial powder. SEM/EDX measurements performed on the white spots (Figs. 4 and 5) confirm these are fractured alumina particles. Moreover, Figs. 4 and 5 show the edges of the larger alumina particles appearing white, indicating particle charging during the characterisation of the coatings using SEM. No other material or inter-metallic was observed from the EDX analysis at the white spots in the SE and BSE images.

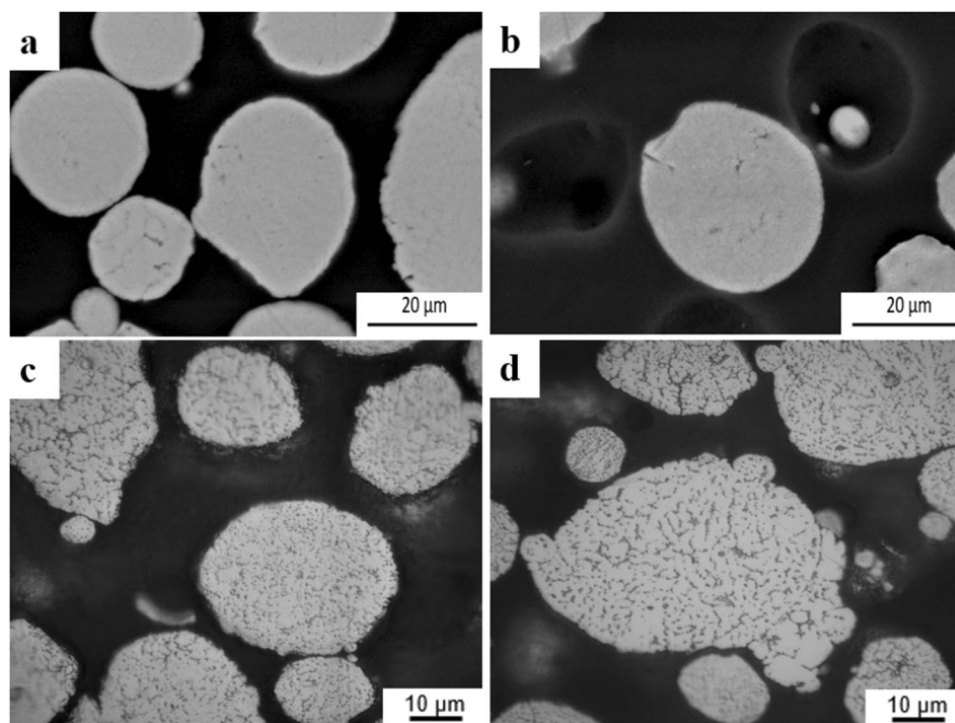
3.1.3 XRD analysis

Fig. 6a shows the XRD profiles of the Al–Mg powders. The XRD diffractograms of Al-7 Mg and Al-10 Mg powders show a single FCC-Al crystal structure detected as $\text{Al}_{0.95}\text{Mg}_{0.05}$ (PDF 01–074–5237). The peaks attributed to this phase indicate a solid solution of Mg in Al matrix. There was no measurable difference between the two diffractograms. Figure 6b shows the XRD profiles of the coatings. There are peaks

related to $\text{Al}_{0.95}\text{Mg}_{0.05}$ (PDF 01–074–5237) and $\alpha\text{-Al}_2\text{O}_3$ (PDF 00–011–0661), of which was added to the powder blends prior to spraying. The XRD analysis detected no other forms of oxides. The evaluated crystallite size of the Al–Mg particles in the unblended feedstock powder and in the composite coatings are presented in the Fig. 6a and b, respectively. The variation in the crystallite size is within the measurement error.

A reduction in the lattice parameters was observed in the Al–Mg coating compared to that of powder in the XRD peaks. The following lattice parameters were measured in the powder: $a=4.059 \text{ \AA}$ and $a=4.065 \text{ \AA}$ for Al-7 Mg and Al-10 Mg alloy powder, respectively. The lattice parameters for the same materials in the coatings were $a=4.046 \text{ \AA}$ and $a=4.046 \text{ \AA}$ for Al-7 Mg and Al-10 Mg alloy coatings, respectively. It is clear that Al-7 Mg and Al-10 Mg show 0.32% and 0.47% reduction in lattice parameters, respectively. The reduction in lattice parameters can qualitatively indicate the presence of compressive residual stresses in the coatings. Also, the

Fig. 2 SE micrographs of the cross-sectioned, colloidal silica polished Al-7 Mg (**a**) and Al-10 Mg (**b**) powders. Optical micrograph of the polished powder reveals dendritic microstructures within the powder both in Al-7 Mg (**c**) and Al-10 Mg (**d**)



higher reduction in lattice parameter suggests the compressive residual stress in Al-10 Mg is likely to be higher than that of Al-7 Mg; however, a detailed analysis using experimental techniques such as X-ray diffraction [24, 25], Raman spectroscopy [26], hole drilling method [25] or nano-indentation technique [27] will be required for future work.

3.2 Hardness and mean free path

The measured nanohardness of the Al-10Mg powder feed-stock (1.22 ± 0.13) GPa is about twice the nanohardness of Al-7Mg (0.56 ± 0.08) GPa. In contrast, after spraying, the

measured nanohardness of the Al-Mg matrix in the composite coatings was 1.87 ± 0.26 GPa and 1.94 ± 0.24 GPa for Al-7Mg and Al-10Mg, respectively, showing a negligible difference. Microhardness measurements were also performed on the AMC coatings, which reflect the composite microhardness of the metal and ceramic. Higher microhardness was obtained in the AMCs, with 2.29 ± 0.06 GPa and 2.82 ± 0.14 GPa for AMC7 and AMC10, respectively. This high hardness is attributed to the addition of the hard phase Al_2O_3 reinforcement particles, as expected. There is a significant decrease in the calculated mean free path between

Fig. 3 SEM image of the blended Al-Mg alloy and alumina; the BSE mode shows Al_2O_3 as a dark phase of angular shape

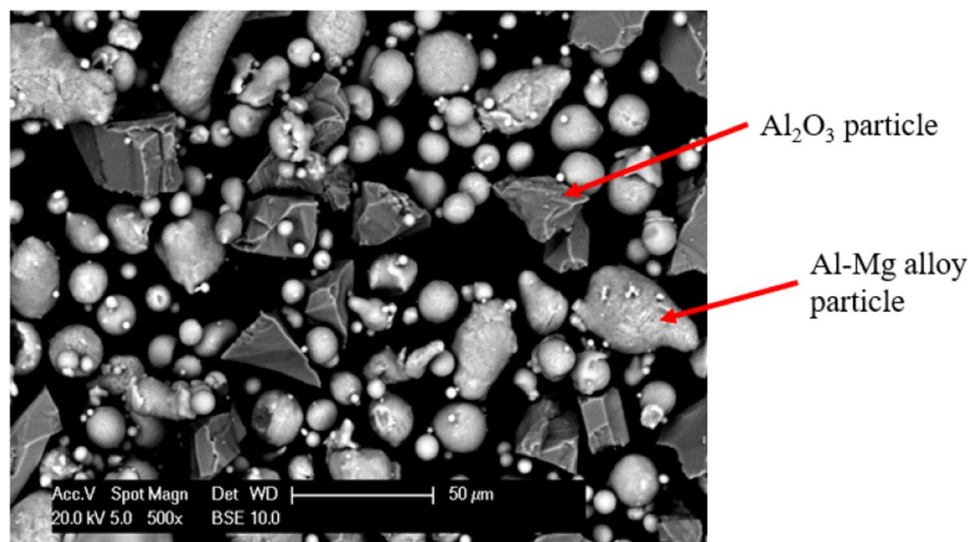


Table 1 Elemental composition of Al–Mg alloy powders evaluated with EDX point scan

Element	Al	Mg	Mn	O
Al-7 Mg (wt%)	91.2	6.7	0.4	1.9
Al-10 Mg (wt%)	87.8	9.4	0.5	2.4

the Al_2O_3 particles from $(10.4 \pm 0.9) \mu\text{m}$ to $(8.6 \pm 0.7) \mu\text{m}$ in the AMC7 and AMC10 coatings, respectively.

3.3 Dry sliding wear testing

The coefficient of friction (μ) against sliding distance for both AMC7 and AMC10 coatings is shown in Fig. 7a. A small variation of μ measured in the first 150 m travelled suggests a bedding-in period; however, then μ remains constant at about 0.5 for both coatings after that point. In general, μ values are similar in both coatings, indicating similar friction behaviour. The specific wear rates of both coatings are displayed in Fig. 7b. AMC7 coatings wore more than AMC10, with ~30% decrease of the wear rate in AMC10 coating.

SEM BSE images of the wear tracks of both coatings are shown in Fig. 8. From the low-magnification images in Fig. 8a and b, the wear track of AMC7 appears wider than that of AMC10. Cracks, grooves, grains pull-out, debris and plastic deformation of the Al–Mg alloy matrix were observed on both coatings. Higher magnification

BSE images are shown in Fig. 8c and d, further revealing these wear features. It is worthy to note that the Al_2O_3 reinforcement particles were observed on the coatings' worn surfaces, which have been likely pulled out of both coatings during the sliding wear test. Overall, there is little difference in the wear features observed on the worn surfaces of the AMC coatings.

The worn surface of the alumina ball tested against both coatings was examined with SEM in the SE and BSE mode and is shown in Fig. 9. This reveals material transferred from the coating to the ball surface, which is likely the Al–Mg matrix having attached to the ball surface during the wear test. The calculated ball wear rates against AMC7 and AMC10 coatings were $(1.11 \pm 0.02) \times 10^{-6} \text{ mm}^3/\text{Nm}$ and $(0.78 \pm 0.02) \times 10^{-6} \text{ mm}^3/\text{Nm}$, respectively. The less aggressive wear behaviour in AMC10 coating also reduces the counterbody wear, which is 30% lower than that against AMC7 coating.

4 Discussion

4.1 Characterisation of the LPCS Al–Mg composite coatings

The densification of AMC coatings developed with the LPCS process is attributed to the addition of the reinforcement phase to the Al–Mg alloy ductile matrix [14]. The tamping and shot-peening effect produced by the hard phase results in compressive stresses on the deposited ductile matrix, which,

Fig. 4 SEM BSE images of AMC7 (a) and AMC10 (b) coatings. The coatings have a dense microstructure with Al_2O_3 reinforcing particles uniformly distributed throughout the coatings. Higher magnification BSE images of AMC7 (c) and AMC10 (d) coatings reveal pores between the alumina particles (indicated by the arrow) embedded within the coatings

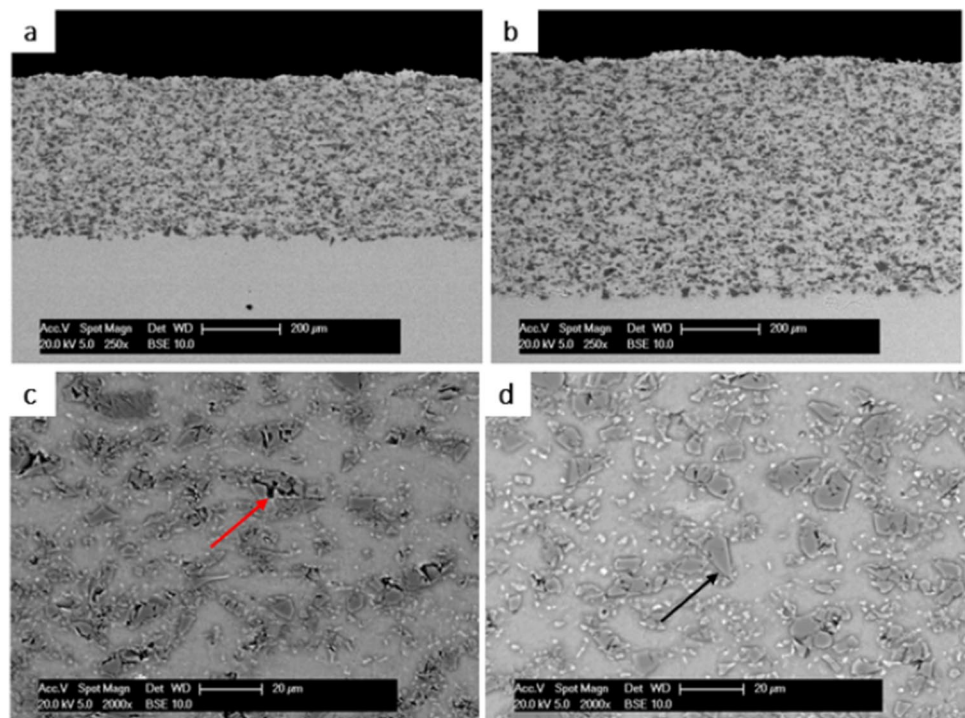
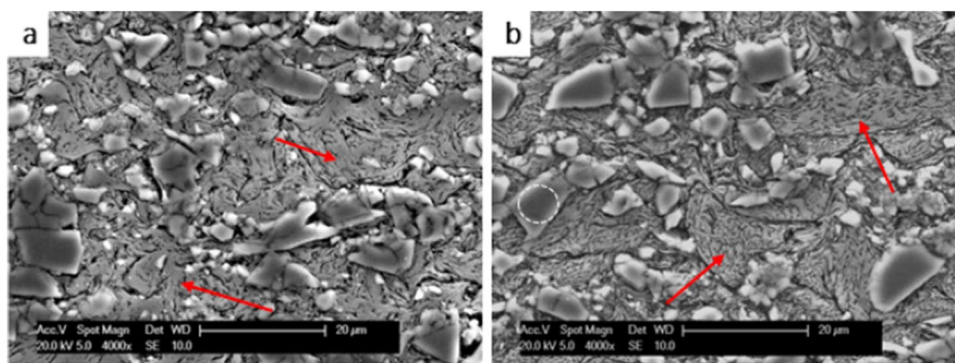


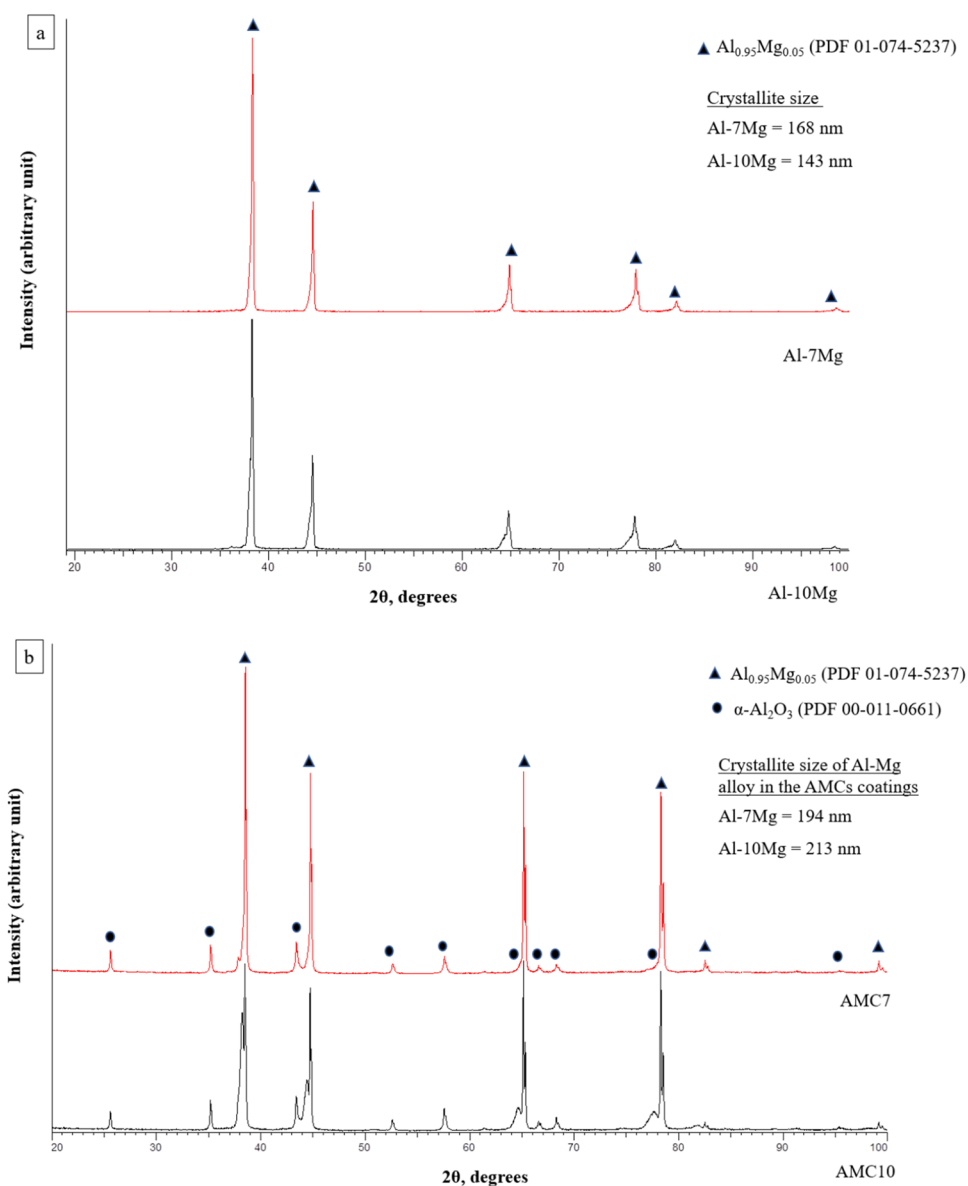
Fig. 5 SE images of the etched cross sections of the AMC7 (a) and AMC10 (b) coatings. The plastically deformed Al–Mg particles are marked with red arrows and the dotted white circle shows the undeformed alumina particles trapped and surrounded by the deformed Al–Mg particles



therefore, increases the denseness of the AMCs [14]. Thus, the addition of the Al_2O_3 reinforcement phase resulted in the successful fabrication of dense AMC7 and AMC10 coatings

using the LPCS. The shot-peening and compaction effect of the Al_2O_3 reinforcing particles also contributed to the severe plastic deformation of the Al–Mg matrix, resulting in the

Fig. 6 a XRD diffractograms of the Al–7 Mg and Al–10 Mg feedstock powders. The crystal structure of the alloy shows a face-centred cubic (FCC) crystal structure of the solid solution of Mg in Al, and b XRD profiles of the composite coatings of AMC7 and AMC10. No phase change or presence of intermetallic compounds was observed. The FCC crystal structure of the alloy was retained, and the α -phase of Al_2O_3 from the blend was detected



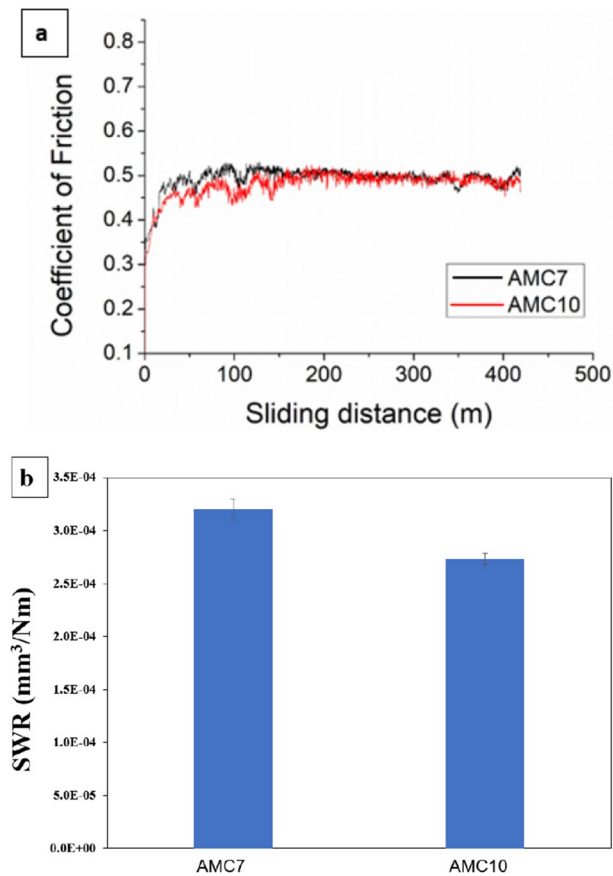


Fig. 7 Coefficient of friction μ against distance travelled (a) and specific wear rate (SWR) for the sliding wear test of both coatings against Al_2O_3 counterbody (b)

mechanical interlocking of the cold-sprayed particles and bonding to the substrate [28], as shown in Figs. 4 and 5. The larger and slower Al_2O_3 particles below the critical deposition velocity do not get incorporated in the coating, and their main effect is in shot peening and compaction.

The concentration of Al_2O_3 ceramic particles retained in the composite coatings AMC7 and AMC10 shows a negligible difference; however, comparing the concentration of Al_2O_3 in the feedstock powder blends and in the composite coatings, a difference emerges suggesting a change in their deposition efficiency. The concentration of Al_2O_3 in the composite coatings ($\sim 20 \text{ wt}\%$) is considerably lower than that in the feedstock powder blends ($40 \text{ wt}\%$). This suggests that during spraying, some of the Al_2O_3 particles bounce off the substrate surface due to their limited plastic deformation. It is expected since the interaction of Al_2O_3 particles with previously embedded Al_2O_3 particles will result in rebounding in the absence of the ductile Al-Mg matrix. At the same time, the retainment of the Al_2O_3 ceramic particles within the composite coatings is due to the deformed Al-Mg particles embedding and trapping the Al_2O_3 particles. The fractured Al_2O_3 particles observed, as seen in Fig. 5, result from the brittle nature of the Al_2O_3 ceramic, which fractured during high velocity impact on the previously deposited Al_2O_3 and Al-Mg particles [15].

In the current study, the same weight fraction of Al_2O_3 was added to the powder blends, sprayed at the same process conditions and yielded different coating thicknesses. The measured composite coating thickness increased by $\sim 50\%$ when sprayed with Al-10 Mg/ Al_2O_3 compared to

Fig. 8 Low-magnification BSE images of the worn surfaces of the AMC7 (a) and AMC10 (b) and higher magnification BSE images of the AMC7 (c) and AMC10 (d) coatings worn surfaces against Al_2O_3 ball, respectively. Cracks, grooves, debris and grains pulled out (red dot) wear features are observed on the worn surfaces

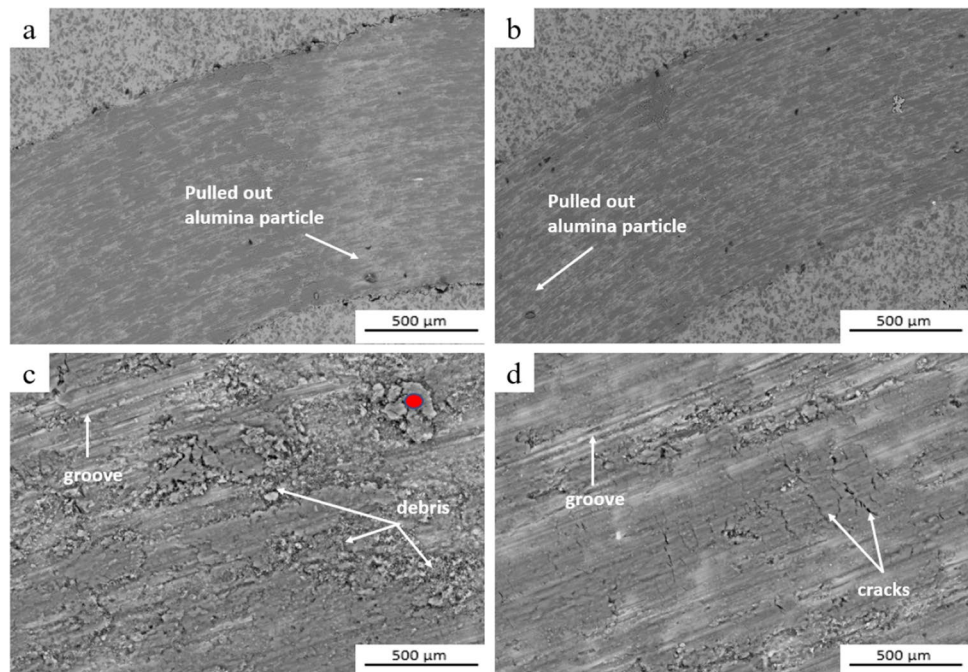
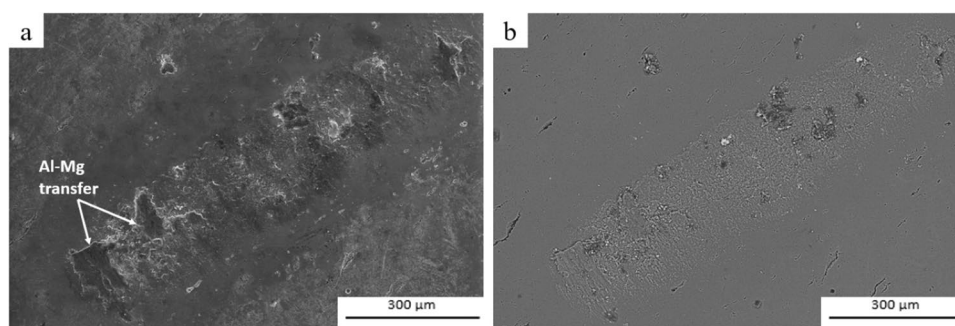


Fig. 9 SE (a) and BSE (b) SEM micrographs of the Al_2O_3 counterbody worn surfaces after sliding wear test against AMC7 composite coatings. The arrows show Al-7 Mg alloy particles attached to the Al_2O_3 ball surface which is the result of material transfer from the coating to the counterbody contact surface. Similar features were observed against AMC10 coatings



Al-7 Mg/ Al_2O_3 . This difference in the composite coating thickness needs further investigation. It should be worth noting that the measured porosity of the composite coatings is $\sim 70\%$ lower in the AMC10 coating as compared to AMC7 coating.

In the XRD analysis performed on the Al–Mg feedstock powders and the LPCS composite coatings, there is no indication that the spray process temperature resulted in the formation of intermetallic compounds or oxides of the Al–Mg alloy matrix in the coating. The temperature of the particles in LPCS process gas stream is well below their melting point [9]. Therefore, as expected, there are no phase changes in the low-pressure cold-sprayed composite coatings, as seen in Fig. 6a and b. In addition, there is no difference in the crystallite size of the Al–Mg alloy matrix.

From our qualitative analysis of lattice parameters, it is likely that Al-10Mg coating was more in compression than that of Al-7Mg. This is also reflected by the lower porosity and higher thickness of the Al-10Mg composite coating. The increase in compressive residual stresses due to higher coating thickness has been reported in HVOF thermal sprayed WC-Co coatings due to more extensive peening stresses [29]. In addition, the higher compressive residual stress of the Al-10Mg alloy coating can also be attributed to its larger particle size (Al-10Mg had a mean particle diameter of $24\text{ }\mu\text{m}$, as shown in Fig. 1c and d when compared to that of Al-7Mg alloy (Al-7Mg had a mean particle diameter of $18.2\text{ }\mu\text{m}$). In a recently published comprehensive review paper, the authors argued that in general, the residual stress increases with an increase in particle diameter due to their higher kinetic energy causing a larger plastic region [30].

4.2 Hardness of the LPCS Al–Mg composite coatings

The measured nanohardness of the Al–Mg alloy powder and the Al–Mg matrices in the composite coatings and the microhardness of the overall AMC coatings reveal the effect of adding Al_2O_3 to the powder blends. The inclusion of Al_2O_3 hard phase reinforcement particles with a nominal hardness

of 10 GPa increased the hardness of the cold-sprayed AMC coatings [15].

In addition, the nanohardness test performed on the Al–Mg matrix in the composite coating was done in order to evaluate, on average, the effect of strain hardening and shot peening/tampering of the reinforcement particles on Al–Mg matrices in the composite coatings. The purpose was to compare the nanohardness of the Al–Mg powder before and after the spray. The high hardness of the Al–Mg matrix in the AMC coatings compared to the feedstock powder particles can be attributed to the plastic deformation resulting from the kinetic energy of the particle on impact and to the tamping/shot-peening effect of the reinforcement particles on the deposited and already deformed Al–Mg matrix. Despite the greater nanohardness of the Al-10Mg alloy powder particle, which is about twice that of Al-7Mg alloy, a negligible difference was observed when comparing the nanohardness of the matrices in the composite coatings. This suggests that the higher percentage increase in the nanohardness of the Al-7Mg alloy in the composite coatings compared to Al-10Mg alloy is likely due to the result of greater strain hardening in the Al-7Mg alloy matrix as a result of its lower powder particle hardness (Fig. 5) [31].

The strengthening mechanism of the LPCS AMC coatings can be explained by the mean free path of the reinforcing particles in the composite coatings. Kouzeli and Mortensen [32], for instance, reported that mean free path has a direct influence on the hardness of MMC coatings; a shorter mean free path would increase the hardness of MMCs coatings. In this work, the greater hardness of AMC10 coating can therefore be attributed to the shorter mean free path of Al_2O_3 in the AMC10 coating. A plausible explanation for the shorter mean free path is the fracturing of the Al_2O_3 particles during the spraying of the AMC10 powder blend, generating a greater number of smaller particles. Moreover, the strength of Al-10Mg alloy particles is twice that of Al-7Mg, and therefore yields greater resistance to the impact of Al_2O_3 particles resulting in the greater fracturing of the embedded Al_2O_3 ceramic particles. Also, the greater fracturing of Al_2O_3 contributed to the lower porosity, in turn enhancing the hardness.

4.3 Wear behaviour of the LPCS Al–Mg composite coatings

The greater mechanical properties of the AMC10 coating can improve its wear resistance properties. The dry sliding wear tests conducted on AMC7 and AMC10 coatings revealed that AMC10 coating wore less than AMC7, as shown in Figure 7b. As expected, the better wear resistance of the AMC10 coating can be attributed to the greater hardness, lower porosity, shorter mean free path [6, 28] and higher compressive residual stress [30]. An increase in compressive residual stress has also been reported to increase the wear resistance of coatings [29]. Therefore, the greater compressive residual stress of the Al–10Mg alloy in the composite coating is likely to contribute to its better wear resistance compared to that of Al–7Mg alloy composite coating.

The wear mechanism of both coatings against the Al_2O_3 counterbody is likely similar since the change in the coefficient of friction μ over distance is similar for both coatings (Fig. 7a). Furthermore, similar wear features such as Al_2O_3 grain pull-out, debris, cracks, grooves, and plastic deformation were observed on the worn surfaces of both composite coatings, as shown in Fig. 8. The features observed on the worn surfaces of the coatings indicate an abrasive wear mechanism, where the Al_2O_3 particles pulled off from the coatings are likely contributing to a significant part of the abrasion of the coating surface. Similar findings have been observed by Hassan et al. [19], confirming that increasing the concentration of alloying elements such as Mg in the matrix fraction of Al–Mg MMCs would increase the hardness and wear resistance of the composite coating.

In addition, the study of Spencer et al. [7] reveals the effect of alloying element in improving the hardness and wear resistance of Al 6061/ Al_2O_3 compared to Al/ Al_2O_3

coatings. The hardness of the AMC coatings in this study is greater than that observed in the work of Spencer et al. [7] and Yu et al. [33], although the coatings are of similar wear behaviour.

In MMC coatings, the major portion of the load from the counterbody is endured by the reinforcement particles, and the resulting volume of material loss is determined by the hardness and toughness of reinforcing particles [34]. As a result, the inclusion of hard phase reinforcing particles decreases the wear rate of AMC coatings. Interestingly, in this study, one significant role of the Al_2O_3 reinforcement particles in the AMC coatings is to support contact stresses resulting from the applied load. This is due to their load-bearing capacity, which in turn enhanced the wear resistance of the coatings. The Al_2O_3 particles were pulled out and entrapped between the alumina counterbody and the coating contact surfaces, resulting in a three-body abrasive wear mechanism (as shown schematically in Fig. 10). The transfer of material to the alumina ball surface, as shown by the SEM micrograph (Fig. 9), indicates adhesive wear mechanism during the dry sliding wear test of the AMC coatings. The wear behaviour of the AMC coatings can be attributed mainly to the abrasion of the coatings' surfaces.

4.4 Future directions

The use of LPCS provides an affordable and portable on-wing technology for the repair of aerospace components such as the floor panel and gearboxes. However, due to its low particle velocity, high-strength materials like Al–Mg alloy are challenging to fabricate with the LPCS process. In this study, thick Al–Mg composite coatings were fabricated, thanks to the inclusion of alumina reinforcement particles

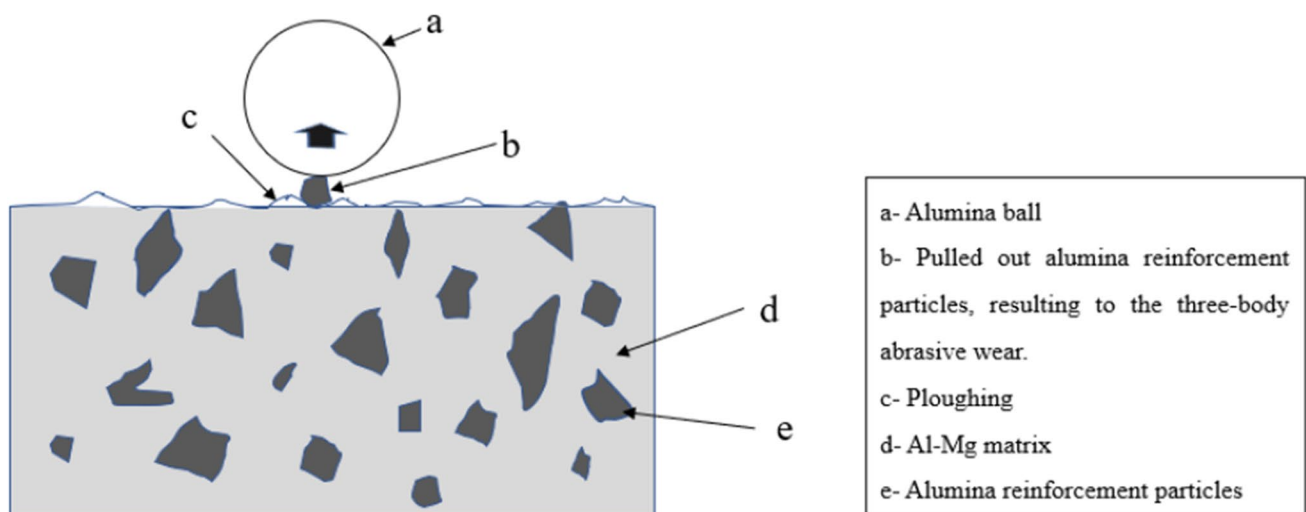


Fig. 10 A schematic representation of a three-body abrasive wear mechanism taking place in Al–Mg alloy composite (AMC) coatings

in the Al–Mg alloy matrix that resulted in the deposition of the coatings using the LPCS technique.

Although it is possible to fabricate Al–Mg alloy coatings using other spraying techniques that do not exhibit any phase transformation or melting and have minimal porosity, it may not always be feasible because of, for example, the expensive gas system (and shortage of helium) in high-pressure cold spraying. However, the hardness values of the AMC coatings in this study could be improved further by cold spraying Al–Mg alloy reinforced with tougher and harder reinforcement particles such as WC, SiC and B₄C particles with LPCS to improve the surface properties of materials where wear is problematic. Finally, further work may include investigating the effect of Mg content at a wider range of Mg wt% on the deposition efficiency, residual stress, wear and hardness of Al–Mg alloy coatings.

5 Conclusion

In this work, Al-7 Mg and Al-10 Mg powders with 40 wt% Al₂O₃ were sprayed with a low-pressure cold spray. The effect of the inclusion of Al₂O₃ in the powder blends and the Mg wt% in the alloy matrix composition on the microstructure, mechanical properties and wear resistance of the composite coatings were investigated. The following conclusions were drawn from the results obtained in this study:

- The addition of Al₂O₃ reinforcing particles to the Al–Mg LPCS feedstock powder enhanced the deposition and bonding of the high-strength Al–Mg alloys due to the shot peening and compaction effect.
- The higher amount of the Mg in the Al–Mg alloy further improved the microstructure of the coatings, as the porosity of AMC10 reduced by ~70% compared to AMC7, with the underlying mechanisms needing further investigation.
- The Al-10 Mg alloy composite coating had a greater hardness of over 23% than the composite coating with Al-7 Mg alloy. In addition, a 17% decrease in the mean free path of the AMC10 coating compared to AMC7 coating contributed to the greater hardness of the AMC10 coating.
- The AMC10 coating had a lower wear rate when compared to AMC7 coating under dry sliding wear test against Al₂O₃ counterbody. This was due to a combined effect of its lower porosity, shorter Al₂O₃ mean free path, likely higher compressive residual stress and higher hardness. The primary wear mechanism is abrasion and it was similar for both coatings, as pulled out Al₂O₃ hard phase particles, debris and grooves were observed on the worn surfaces of both composite coatings. Nevertheless, AMC7 coating suffered a higher degree of material loss. The

Al₂O₃ particles were pulled out and entrapped between the alumina counterbody and the composite coating contact surfaces, resulting in a three-body abrasion.

Acknowledgements The authors acknowledge financial support from the Engineering and Physical Sciences Research Council [EP/N50970X/1]. The authors also acknowledge John Kirk at the University of Nottingham for conducting the cold spray experiments, and the Nanoscale and Microscale Research Centre (nmRC) at the University of Nottingham for the use of SEM equipment.

Author contribution C. J. Akisin: Investigation, formal analysis, writing—original draft, writing—review & editing. F. Venturi: supervision, formal analysis, writing—review & editing. M. Bai: writing—review & editing, software. C. Bennett: Supervision, project administration. T. Hussain: supervision, project administration, conceptualization, writing—review & editing.

Funding This work was supported by the Engineering and Physical Sciences Research Council [EP/N50970X/1] with Cletus J. Akisin being the recipient as a PhD researcher.

Data availability Not applicable.

Code availability Not applicable.

Declarations

Ethics approval Not applicable.

Consent to participate Not applicable.

Consent for publication Not applicable.

Competing interests The authors declare no competing interests.

Open Access This article is licensed under a Creative Commons Attribution 4.0 International License, which permits use, sharing, adaptation, distribution and reproduction in any medium or format, as long as you give appropriate credit to the original author(s) and the source, provide a link to the Creative Commons licence, and indicate if changes were made. The images or other third party material in this article are included in the article's Creative Commons licence, unless indicated otherwise in a credit line to the material. If material is not included in the article's Creative Commons licence and your intended use is not permitted by statutory regulation or exceeds the permitted use, you will need to obtain permission directly from the copyright holder. To view a copy of this licence, visit <http://creativecommons.org/licenses/by/4.0/>.

References

1. I.A. Ibrahim, F.A. Mohamed, E.J. Lavernia, Particulate reinforced metal matrix composites - a review. *J. Mater. Sci.* **26**, 1137–1156 (1991). <https://doi.org/10.1007/BF00544448>
2. X. Xie, C. Chen, Z. Chen, W. Wang, S. Yin, G. Ji, H. Liao, Achieving simultaneously improved tensile strength and ductility of a nano-TiB₂/AlSi10Mg composite produced by cold spray additive manufacturing. *Compos. Part B Eng.* 108404 (2020). <https://doi.org/10.1016/j.compositesb.2020.108404>

3. S. Yin, Y. Xie, J. Cizek, E.J. Ekoi, T. Hussain, D.P. Dowling, R. Lupoi, Advanced diamond-reinforced metal matrix composites via cold spray: properties and deposition mechanism. *Compos. Part B Eng.* **113**, 44–54 (2017). <https://doi.org/10.1016/j.compositesb.2017.01.009>
4. S.R. Bakshi, V. Singh, K. Balani, D.G. McCartney, S. Seal, A. Agarwal, Carbon nanotube reinforced aluminum composite coating via cold spraying. *Surf. Coatings Technol.* **202**, 5162–5169 (2008). <https://doi.org/10.1016/j.surfcoat.2008.05.042>
5. X. Xie, S. Yin, R. Raoelison, C. Chen, C. Verdy, W. Li, G. Ji, Z. Ren, H. Liao, Al matrix composites fabricated by solid-state cold spray deposition: a critical review. *J. Mater. Sci. Technol.* **86**, 20–55 (2021). <https://doi.org/10.1016/j.jmst.2021.01.026>
6. N.M. Melendez, A.G. McDonald, Development of WC-based metal matrix composite coatings using low-pressure cold gas dynamic spraying. *Surf. Coat. Technol.* **214**, 101–109 (2013). <https://doi.org/10.1016/j.surfcoat.2012.11.010>
7. K. Spencer, D.M. Fabijanic, M.X. Zhang, The use of Al-Al₂O₃ cold spray coatings to improve the surface properties of magnesium alloys. *Surf. Coat. Technol.* **204**, 336–344 (2009). <https://doi.org/10.1016/j.surfcoat.2009.07.032>
8. F. Nturanabo, L. Masu, J. Baptist Kirabira, Novel applications of aluminium metal matrix composites. *Alum. Alloy. Compos.*, IntechOpen. (2020). <https://doi.org/10.5772/intechopen.86225>
9. T. Schmidt, H. Assadi, F. Gärtner, H. Richter, T. Stoltenhoff, H. Kreye, T. Klassen, From particle acceleration to impact and bonding in cold spraying. *J. Therm. Spray Technol.* **18**, 794–808 (2009). <https://doi.org/10.1007/s11666-009-9357-7>
10. A. Sova, A. Papyrin, I. Smurov, Influence of ceramic powder size on process of cermet coating formation by cold spray. *J. Therm. Spray Technol.* **18**, 633–641 (2009). <https://doi.org/10.1007/s11666-009-9359-5>
11. K.J. Hodder, H. Izadi, A.G. McDonald, A.P. Gerlich, Fabrication of aluminum-alumina metal matrix composites via cold gas dynamic spraying at low pressure followed by friction stir processing. *Mater. Sci. Eng. A.* **556**, 114–121 (2012). <https://doi.org/10.1016/j.msea.2012.06.066>
12. A. Moridi, S.M. Hassani-Gangaraj, M. Guagliano, M. Dao, Cold spray coating: review of material systems and future perspectives. *Surf. Eng.* **30**, 369–395 (2014). <https://doi.org/10.1179/1743294414Y.0000000270>
13. L. He, M. Hassani, A review of the mechanical and tribological behavior of cold spray metal matrix composites. *J. Therm. Spray Technol.* (2020). <https://doi.org/10.1007/s11666-020-01091-w>
14. Y.T.R. Lee, H. Ashrafizadeh, G. Fisher, A. McDonald, Effect of type of reinforcing particles on the deposition efficiency and wear resistance of low-pressure cold-sprayed metal matrix composite coatings. *Surf. Coat. Technol.* **324**, 190–200 (2017). <https://doi.org/10.1016/j.surfcoat.2017.05.057>
15. K.J. Hodder, J.A. Nychka, A.G. McDonald, Comparison of 10 µm and 20 nm Al-Al₂O₃ metal matrix composite coatings fabricated by low-pressure cold gas dynamic spraying. *J. Therm. Spray Technol.* **23**, 839–848 (2014). <https://doi.org/10.1007/s11666-014-0094-1>
16. A.B. Spierings, K. Dawson, K. Kern, F. Palm, K. Wegener, SLM-processed Sc- and Zr- modified Al-Mg alloy: mechanical properties and microstructural effects of heat treatment. *Mater. Sci. Eng. A.* **701**, 264–273 (2017). <https://doi.org/10.1016/j.msea.2017.06.089>
17. T. Yuan, Z. Yu, S. Chen, M. Xu, X. Jiang, Loss of elemental Mg during wire + arc additive manufacturing of Al-Mg alloy and its effect on mechanical properties. *J. Manuf. Process.* **49**, 456–462 (2020). <https://doi.org/10.1016/j.jmapro.2019.10.033>
18. B.H. Lee, S.H. Kim, J.H. Park, H.W. Kim, J.C. Lee, Role of Mg in simultaneously improving the strength and ductility of Al-Mg alloys. *Mater. Sci. Eng. A.* **657**, 115–122 (2016). <https://doi.org/10.1016/j.msea.2016.01.089>
19. A.M. Hassan, A. Alrashdan, M.T. Hayajneh, A.T. Mayyas, Wear behavior of Al-Mg-Cu-based composites containing SiC particles. *Tribol. Int.* **42**, 1230–1238 (2009). <https://doi.org/10.1016/j.triboint.2009.04.030>
20. P. Chivavibul, M. Watanabe, S. Kuroda, K. Shinoda, Effects of carbide size and Co content on the microstructure and mechanical properties of HVOF-sprayed WC-Co coatings. *Surf. Coat. Technol.* **202**, 509–521 (2007). <https://doi.org/10.1016/j.surfcoat.2007.06.026>
21. K.S. Al-Hamdani, J.W. Murray, T. Hussain, A.T. Clare, Heat-treatment and mechanical properties of cold-sprayed high strength Al alloys from satellited feedstocks. *Surf. Coat. Technol.* **374**, 21–31 (2019). <https://doi.org/10.1016/j.surfcoat.2019.05.043>
22. P.H. Shipway, The role of test conditions on the microabrasive wear behaviour of soda-lime glass, in: *Wear*, (Elsevier Sequoia SA, 1999), pp. 191–199. [https://doi.org/10.1016/S0043-1648\(99\)00187-8](https://doi.org/10.1016/S0043-1648(99)00187-8)
23. A. Sabard, T. Hussain, Inter-particle bonding in cold spray deposition of a gas-atomised and a solution heat-treated Al 6061 powder. *J. Mater. Sci.* **54**, 12061–12078 (2019). <https://doi.org/10.1007/s10853-019-03736-w>
24. Z. Zhang, F. Liu, E.H. Han, L. Xu, P.C. Uzoma, Effects of Al₂O₃ on the microstructures and corrosion behavior of low-pressure cold gas sprayed Al 2024-Al₂O₃ composite coatings on AA 2024-T3 substrate. *Surf. Coat. Technol.* **370**, 53–68 (2019). <https://doi.org/10.1016/j.surfcoat.2019.04.082>
25. T.A. Owoseni, M. Bai, N. Curry, E.H. Lester, D.M. Grant, T. Hussain, Residual stress measurement of suspension HVOF-sprayed alumina coating via a hole-drilling method. *J. Therm. Spray Technol.* **29**, 1339–1350 (2020). <https://doi.org/10.1007/s11666-020-01072-z>
26. Z. Zou, J. Donoghue, N. Curry, L. Yang, F. Guo, P. Nylén, X. Zhao, P. Xiao, A comparative study on the performance of suspension plasma sprayed thermal barrier coatings with different bond coat systems. *Surf. Coat. Technol.* **275**, 276–282 (2015). <https://doi.org/10.1016/j.surfcoat.2015.05.006>
27. L.N. Zhu, B.S. Xu, H.D. Wang, C.B. Wang, Measurement of residual stresses using nanoindentation method. *Crit. Rev. Solid State Mater. Sci.* **40**, 77–89 (2015). <https://doi.org/10.1080/10408436.2014.940442>
28. E. Irissou, J.G. Legoux, B. Arsenaault, C. Moreau, Investigation of Al-Al₂O₃ cold spray coating formation and properties. *J. Therm. Spray Technol.* (2007): pp. 661–668. <https://doi.org/10.1007/s11666-007-9086-8>
29. W. Luo, U. Selvadurai, W. Tillmann, Effect of residual stress on the wear resistance of thermal spray coatings. *J. Therm. Spray Technol.* **25**, 321–330 (2016). <https://doi.org/10.1007/s11666-015-0309-0>
30. A. Fardan, C.C. Berndt, R. Ahmed, Numerical modelling of particle impact and residual stresses in cold sprayed coatings: a review. *Surf. Coat. Technol.* **409**, 126835 (2021). <https://doi.org/10.1016/j.surfcoat.2021.126835>
31. B. Jodoin, L. Ajdelsztajn, E. Sansoucy, A. Zúñiga, P. Richer, E.J. Lavernia, Effect of particle size, morphology, and hardness on cold gas dynamic sprayed aluminum alloy coatings. *Surf. Coat. Technol.* **201**, 3422–3429 (2006). <https://doi.org/10.1016/j.surfcoat.2006.07.232>
32. M. Kouzeli, A. Mortensen, Size dependent strengthening in particle reinforced aluminium. *Acta Mater.* **50**, 39–51 (2002). [https://doi.org/10.1016/S1359-6454\(01\)00327-5](https://doi.org/10.1016/S1359-6454(01)00327-5)
33. M. Yu, X.K. Suo, W.Y. Li, Y.Y. Wang, H.L. Liao, Microstructure, mechanical property and wear performance of cold sprayed Al5056/SiCp composite coatings: effect of reinforcement content. *Appl. Surf. Sci.* **289**, 188–196 (2014). <https://doi.org/10.1016/j.apsusc.2013.10.132>
34. N.M. Melendez, V.V. Narulkar, G.A. Fisher, A.G. McDonald, Effect of reinforcing particles on the wear rate of low-pressure cold-sprayed WC-based MMC coatings. *Wear* **306**, 185–195 (2013). <https://doi.org/10.1016/j.wear.2013.08.006>